Electronic Supplementary Material (ESI) for ChemComm.

Electronic Supplemental Information: Pressure-induced metallization and 3d-like behavior in TcS_2

Dean Sayre,[†,‡] Emily Siska,[†,‡] G. Alexander Smith,[†,¶] Nicholas Chang,[¶] Frederic Poineau,[¶] Changyong Park,[§] Craig Schwartz,[†] Keith V. Lawler,[*,†] and Ashkan Salamat[*,†,‡]

†*Nevada Extreme Conditions Laboratory, University of Nevada, Las Vegas, Las Vegas, Nevada 89154, USA*

‡*Department of Physics & Astronomy, University of Nevada Las Vegas, Las Vegas, Nevada 89154, USA*

¶*Department of Chemistry & Biochemistry, University of Nevada Las Vegas, Las Vegas, Nevada 89154, USA*

§*X-ray Science Division, Argonne National Laboratory, Illinois 60439, USA*

E-mail: keith.lawler@unlv.edu; salamat@physics.unlv.edu

Experimental

Caution! *^{99}Tc is a weak β emitter ($E_{max} = 293$ KeV, $t_{1/2} = 2.1\ 10^5$ y). Any manipulation of the material was performed in a posted radiochemical laboratory. All efforts followed locally approved handling and monitoring procedures for the specific radioisotope. Details on the containment of samples can be found in previous works.*[1]

TcS_2 samples were prepared by UNLV Radiochemistry following a reaction between the elements described elsewhere.[2] Powder samples were loaded into a diamond anvil cell (DAC) with 250 μm culet diamonds using rhenium gaskets. Samples were either gas loaded with argon or alumina. Alumina was used to create a non-hydrostatic environment; maximizing stress on the system to induce metallization and pressure induced amorphization. Temperature was determined using optical pyrometry. However, the coupling efficiency changed as a function of time, indicating a change in emissivity. This would have rendered optical pyrometry unreliable thus it is not reported here. Offline Raman spectra were taken at each pressure point and before and after each heating. Diffraction images were collected with either a Pilatus 1M, MAR345, and MAR165 CDD detector. To reduce the collected XRD data we used Dioptas,[3] and for full Rietveld and Le Bail refinments we used GSAS.[4] XANES calculations were performed with the Finite Difference Method Near Edge Structure (FDMNES)[5,6] which utilizes Density Functional Theory (DFT). The TcS_2 XANES were aligned to metallic Tc.

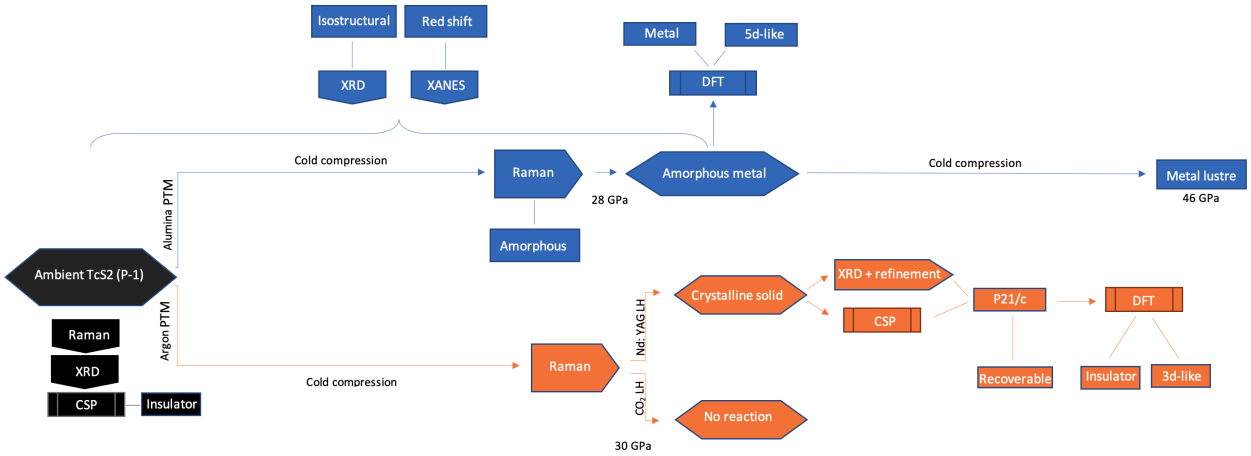

Figure S1: The above flowchart describes the two separate experiments performed on TcS_2 samples. In the first experiment (blue arrows and labels) TcS_2 was loaded with an alumina PTM, cold compressed and probed with XRD, XANES, and Raman throughout the pressure range. DFT calculations characterize this phase as an amorphous metal which exhibits a metallic lustre near 46 GPa. In the second experiment (orange arrows and labels), the sample was loaded with argon and compressed and laser heated. We found no reaction upon laser heating with CO_2. Upon using a Nd: YAG laser, Raman and XRD analysis support a new phase with distinct Ramam modes and Bragg features. CSP and DFT calculations were performed to characterize this new phase which is a negative charge-transfer insulator. Further, decompression experiments support evidence of recoverability.

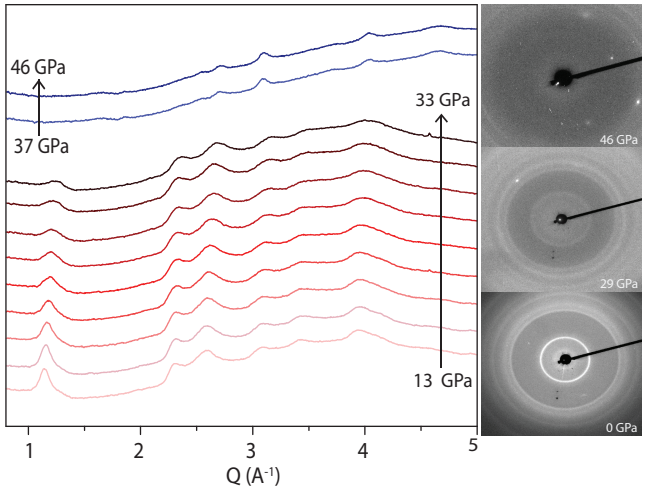

Figure S2: Left: Complimentary XRD of room temperature compression of TcS_2 (blue and red correspond to XANES blue and red shown in main text). Data in blue was collected at $\lambda = 0.4143$ Å and red data was collected at $\lambda = 0.4959$ Å, shown in Q space in order to plot together. Right: Two-dimensional image of diffraction patterns of TcS_2 recorded at HPCAT (APS Sector 16, ANL).

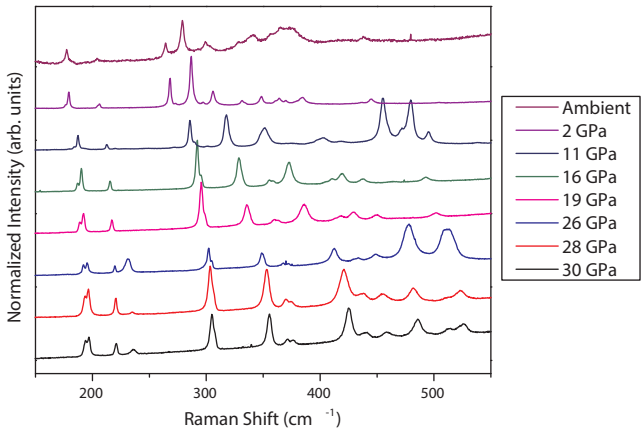

Figure S3: A stack plot of the raw Raman spectra taken upon decompression of a laser-heated transformed $P2_1/c$ TcS_2 sample. In general, a softening of the modes is observed, with the features between 300–400 cm^{-1} at 30 GPa coalescing around 300 cm^{-1} at ambient.

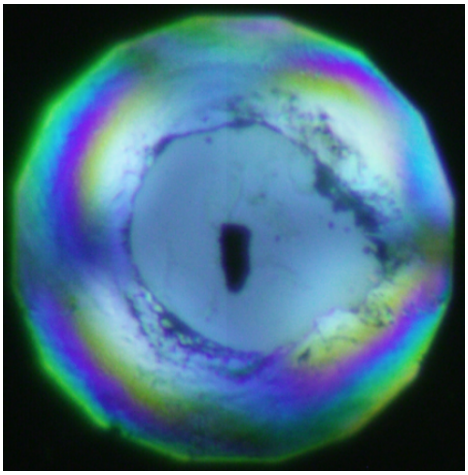

Figure S4: Image of the recovered arsenopyrite phase. This transformed arsenopyrite phase has a dull, black color.

Theory

Under the assumption of no disproportionation, crystal structure prediction (CSP) simulations were performed to determine candidate ambient and high pressure phases of TcS_2 using the evolutionary algorithm USPEX.[7–9] Individual searches for non-magnetic structures with 1-4 formula units (f.u.) per unit cell were considered with 50 structures in the initial generation and 20 structures in subsequent generations. The predicted structures were optimized using plane-wave density functional theory (DFT) with VASP 5.4.4 (Vienna ab initio Simulation Package) with a 600 eV plane wave cutoff energy.[10] Enthalpically favorable structures produced by the crystal structure searches were subsequently re-optimized twice to refine the structure while minimizing Pulay stress. In those calculations, the Brillouin zone was represented by an automatically generated Γ-centered k-point grid with 0.3 and 0.15 $Å^{-1}$ resolution. The convergence criterion for the energy and forces were 10^{-7} eV and -10^{-4} $eVÅ^{-1}$, respectively. Structural analysis and visualization was performed with VESTA.[11] The strongly constrained and appropriately normed meta-GGA functional with the revised Vydrov–van Voorhis nonlocal correlation functional for van der Waals interactions (SCAN-rVV10) was used in all calculations.[12–14] Supplementary calculations were also performed with the and PBE functional.[15] The projector augmented wave (PAW)[16,17] pseudopotentials were used to represent the ionic cores with valence configurations $3p^6 5s^2 4d^5$ for technetium and $3s^2 3p^4$ for sulfur. The lattice vibrational modes were obtained at the Γ-point using finite differences and analyzed with the phonopy python package.[18] To evaluate if magnetic ordering could occur in a given structure, a single parameter Hubbard $+U$ correction was applied to the transition metal d states.

Both measured[†] and predicted crystallographic studies of TcS_2 at high pressures are shown in Table 1. The algorithm resulted in three monoclinic cells and a single orthorhomic cell. For each prediction the symmetry, enthalpy relative to the enthalpically favorable structure, lattice constants, volume, Wyckoff sites, and atomic positions are shown. The enthalpically favorable structure is of the arsenopyrite type ($P2_1/c$) in four formula units per unit cell.

Table S1: Relative enthalpies and crystallographic information for the enthalpically favorable structures predicted by CSP in 1–4 formula units at 20 GPa. Also shown is the Rietveld-refined parameters of the high pressure phase of $TcS_2^{\dagger}$ measured from powder-crystal x-ray diffraction at 30 GPa, and the optimized $P\bar{1}$ structure predicted via. CSP at ambient.

Symmetry & Pressure (GPa)	ΔH (meV/f.u.)	Lattice (Å, °)	Volume (Å^3/f.u.)	Atom (Wyckoff site)	x	y (fractional)	z
Cm (8)	1035	$a = 10.63$	43.32	Tc (2a)	0.1605	0.5000	0.8930
20 GPa		$b = 3.098$		S1 (2a)	0.8998	0.0000	0.6530
		$c = 5.544$		S2 (2a)	0.0905	0.0000	0.4683
		$\alpha = \gamma = 90.00$					
		$\beta = 151.70$					
$Pnmn$ (58)	313	$a = 4.827$	41.35	Tc (2a)	0.0000	0.0000	0.0000
20 GPa		$b = 3.037$		S (4g)	0.6690	0.5000	0.8760
		$c = 5.643$					
		$\alpha = \beta = \gamma = 90$					
$C2/m$ (12)	818	$a = 8.768$	42.11	Tc1 (2i)	0.1991	0.0315	0.0218
20 GPa		$b = 3.034$		Tc2 (1a)	0.5195	0.3733	0.5785
		$c = 4.844$		S1 (2i)	0.2750	0.4952	0.7133
		$\alpha = 89.897$		S2 (2i)	0.1062	0.5760	0.3372
		$\beta = 95.586$		S3 (2i)	0.4357	0.9158	0.2364
		$\gamma = 80.193$					
$P2_1/c$ (14)	0	$a = 5.617$	41.66	Tc (4e)	0.7271	0.4999	0.7121
20 GPa		$b = 5.630$		S1 (4e)	0.1581	0.1194	0.3637
		$c = 5.677$		S2 (4e)	0.6621	0.3717	0.3168
		$\alpha = \gamma = 90.00$					
		$\beta = 111.90$					
$P2_1/c^{\dagger}$ (14)	-	$a = 5.567$	40.44	Tc (4e)	0.2761	0.0081	0.2921
30 GPa		$b = 5.587$		S1 (4e)	0.8453	0.6197	0.6359
		$c = 5.627$		S2 (4e)	0.3350	0.8753	0.6701
		$\alpha = \gamma = 90.00$					
		$\beta = 112.42$					
$P\bar{1}$ (2)	-	$a = 6.367$	52.99	Tc1 (1a)	0.93156	0.68955	0.48900
0 GPa		$b = 6.457$		Tc2 (1a)	0.05727	0.30805	0.50712
		$c = 6.628$		Tc3 (1a)	0.50598	0.71278	0.49561
		$\alpha = 62.844$		Tc4 (1a)	0.48282	0.28471	0.50048
		$\beta = 103.57$		S1 (1a)	0.63340	0.69089	0.20781
		$\gamma = 118.87$		S2 (1a)	0.35546	0.30657	0.78825
				S3 (1a)	0.17098	0.71941	0.23635
				S4 (1a)	0.81792	0.27817	0.75974
				S5 (1a)	0.85115	0.82672	0.72362
				S6 (1a)	0.13772	0.17085	0.27252
				S7 (1a)	0.31447	0.81137	0.69731
				S8 (1a)	0.67433	0.18618	0.29886

The same information is tabulated for the Rietveld refined high pressure structure measured during XRD runs. Calculations overestimate cell edges by 0.76-0.88%, underestimate β by 0.46%, and overestimates the unit cell volume per formula unit by roughly 3%. The resulting low enthalpy structures in each formula unit are shown in Figure 5, along with the enthalpically favorable $P\bar{1}$ structure predicted at 0 GPa. Of the four predicted high pressure structures, one is of the layered type (Cm) with the remaining structures extended as shown.

The differences in Tc–Tc and S–S distances between the predicted and Rietveld refined structures of $P2_1/c$ TcS_2 are shown in Figure 7. From this perspective the existence of nearest-neighbor alternating Tc-Tc distances is apparent, depicted by the red dashed lines in Angstroms. Alternating bonds differ by roughly 0.56% and 3.0%. Nearest-neighbor S–S distances between the two version are also compared. Calculations underestimate this by roughly 3.0%.

To explore magnetic ordering in the arsenopyrite phase of TcS_2 we determined the Hubbard $+U$ term on Tc d-electrons using the linear response Ansatz of Cococcioni and De Giron-

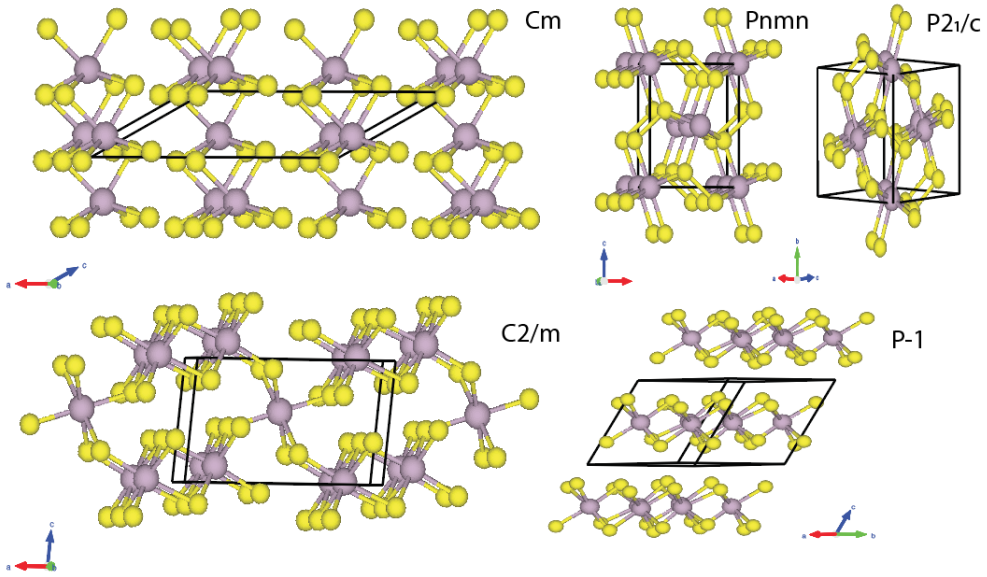

Figure S5: [19] Resulting energetically favorable crystal structures predicted by CSP in four formula units at 0 and 20 GPa. The resulting crystal structures belong to the symmetry groups Cm, $C2/m$, $Pnmn$, and $P2_1/c$ in 1-4 f.u. CSP was also performed at 0 GPa, and is shown below, which confirms the $P\bar{1}$ symmetry measured by Lamfers et al.[20] by means of single crystal XRD.

coli[21], and implemented the GGA+U_{eff} calculations using the formalism derived by Dudarev et al.[22], where $U_{eff} = U - J$. Initially, the on-site exchange parameter (J) is set to zero and the on-site Coulomb parameter (U) is determined to be $U = 2.9eV$ using the local density approximation. A single ferromagnetic and 5 antiferromagnetic Tc spin orderings were attempted consistent with the monoclinic parent lattice of $P2_1/c$ TcS_2, however no magnetic solution was found near the calculated value of U, using the SCAN rVV10 functional. It isn't until $U = 5$ and $U = 6$ that antiferromagntic and ferromagnetic orderings are found using the selected GGA scheme, respectively. In the former case two antiferromagnetic orderings are roughly 200 meV more enthalpically favorable with a magnetic moment-per Tc atom of 0.423 μ_B for both magnetic solutions, while in the latter a non-magnetic phase is enthalpically prevalent. Typically in the Group 7 oxides a large value for the Coulomb term is necessary,[23,24] so it isn't surprising that large values of U are suitable for these systems. Structural implications imply that spin-ordering restores equidistant Tc-Tc distances, thus to this extent calculations involving spin-ordering including a Hubbard U term is ignored as the measured structure was found to exhibit alternating Tc distances.

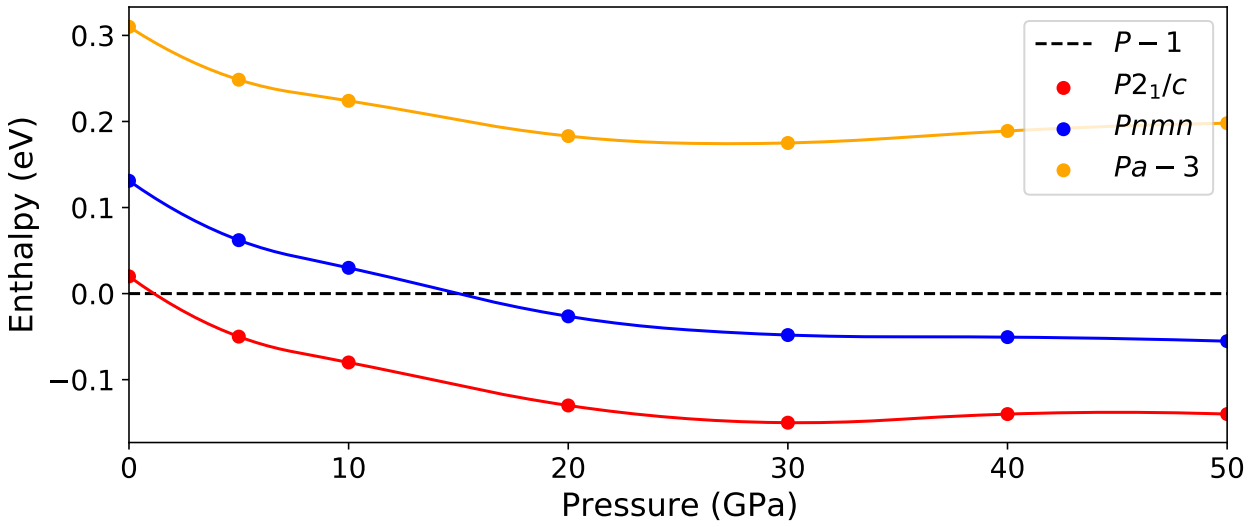

Figure S6: A comparison of the enthalpy as a function of pressure for the $P\bar{1}$, arsenopyrite ($P2_1/c$), marcasite ($Pmnm$), and pyrite ($Pa\bar{3}$) phases of TcS_2. Calculations show the high pressure arsenopyrite phase becomes stable versus the ambient $P\bar{1}$ phase by 5 GPa.

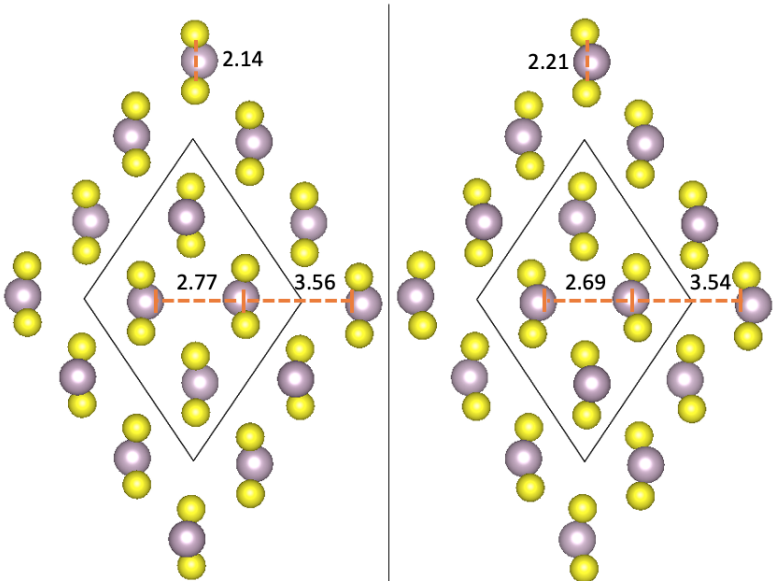

Figure S7: Comparison of the predicted lowest enthalpy (left) and Rietveld refined (right) crystal structures at 20 GPa.

The finite difference method was applied to determine the phonon relations of $P\bar{1}$ TcS_2, resulting in $\Gamma = 18A_g + 18A_u$ vibrational modes. Table 2 compares the measured Raman activity with the 18 calculated raman-active modes. It is apparent that including a Hubbard Coulomb term of 6 eV increases agreement for highly active modes.

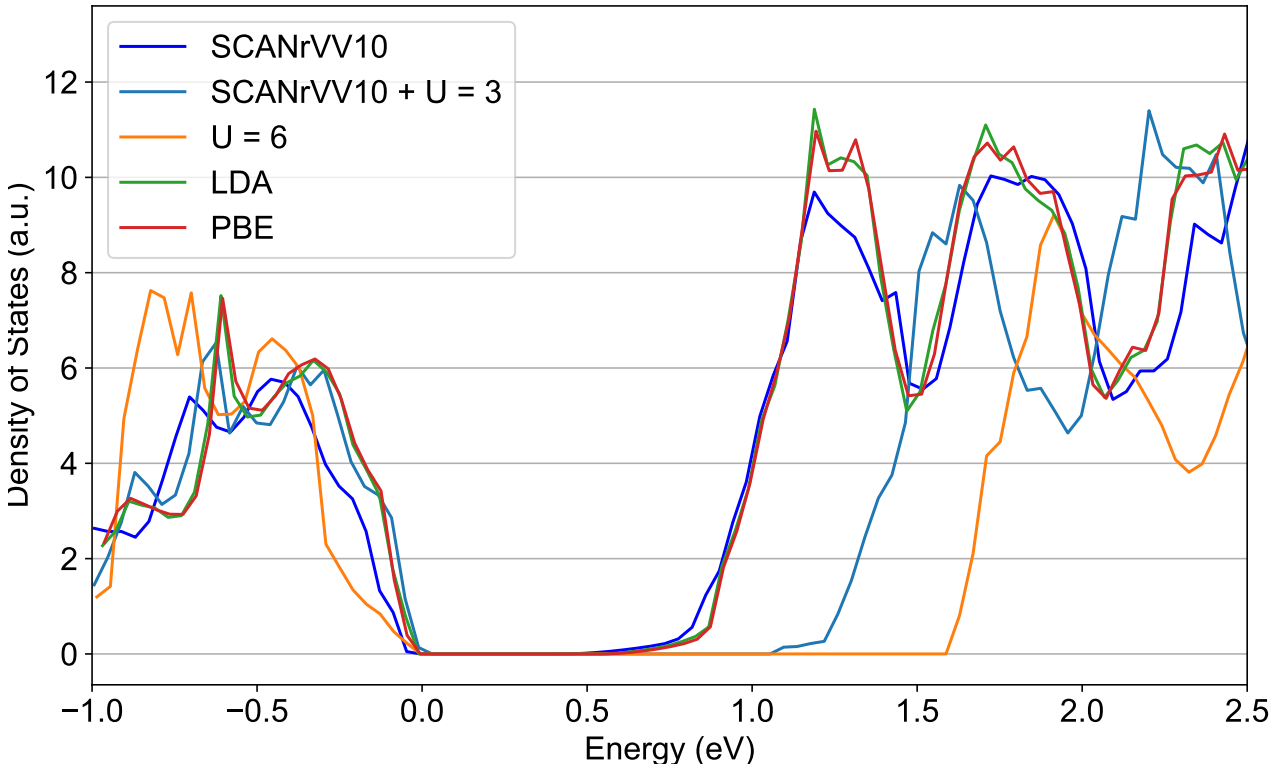

Figure S8: Electronic density of states calculated with SCAN rVV10, LDA, and PBE functionals at 0 GPa. Also shown are the DOS including a Hubbard U term for U = 3 and 6 eV. Calculations including a U term were performed using the SCAN rVV10 functional. In the figure, 0 eV corresponds to the fermi-level (ϵ_f). In the conduction band, the relative energy shifts prominent when increasing the Hubbard U term, and the difference in DOS across the three sampled functionals is more apparent for SCAN rVV10. In the valence band inclusion of the Hubbard U term plays an interesting role: First orbitals shift closer towards ϵ_f for $U = 3$ eV then retreat away when $U = 6$ eV. This is likely the reason for an availability of magnetic ordering for such a high value of the Coulomb correction term.

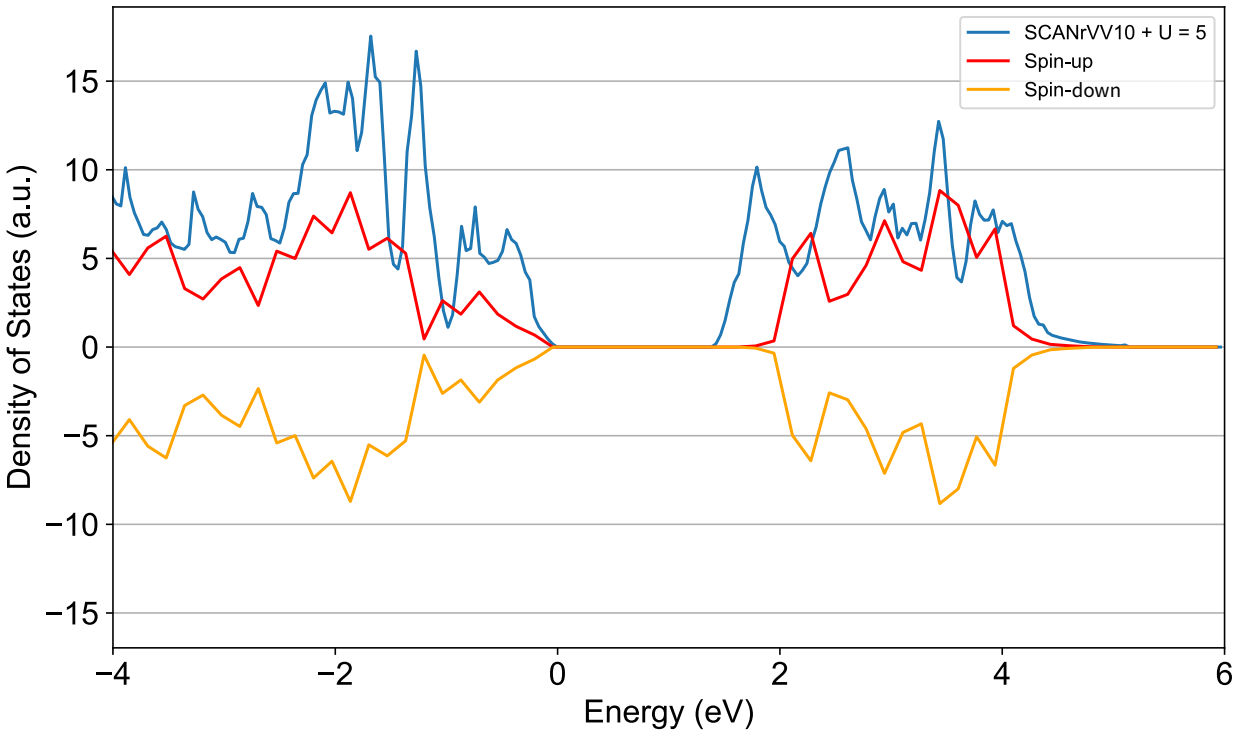

Figure S9: Electronic density of states at 0 GPa calculated with the SCAN rVV10 functional including a Hubbard U term. The spin-up (red) and spin-down (orange) channels correspond to an anti-ferromagnetic ordering. The blue channel is absent of magnetic ordering. All channels use a U term of 5 eV. Notice that the conduction band shifts up nearly three-quarters of an eV. This is likely due to the restoration of equidistant Tc–Tc distances.

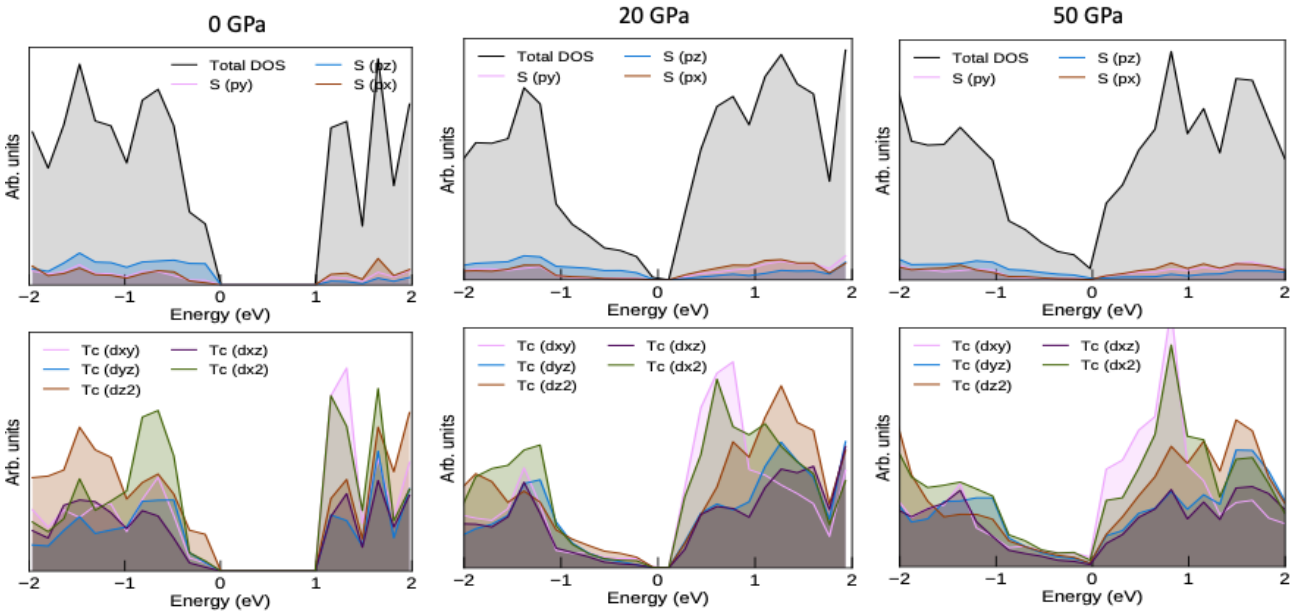

Figure S10: Orbital decomposed charge density of states for $P\bar{1}$ TcS_2 at 0, 20, and 50 GPa. Contributions to the DOS for S and Tc are shown at the top and bottom, respectively.

Table S 2: Measured and computed Raman frequencies of $P\bar{1}$ TcS_2 at 0 GPa which are assigned 18 gerade modes (A_g). Calculations were performed using the SCAN+rVV10 functional with and without a Hubbard U term of 6 eV.

Experiment (cm^{-1})	SCAN+rVV10 (cm^{-1})	SCAN+rVV10+U (cm^{-1})
147	159	153
161	169	163
179	188	180
185	200	185
X	255	230
246	272	250
265	276	262
X	297	281
X	308	288
297	309	298
303	320	310
314	327	318
322	351	339
362	367	361
X	379	372
402	418	406
420	433	423
440	449	436

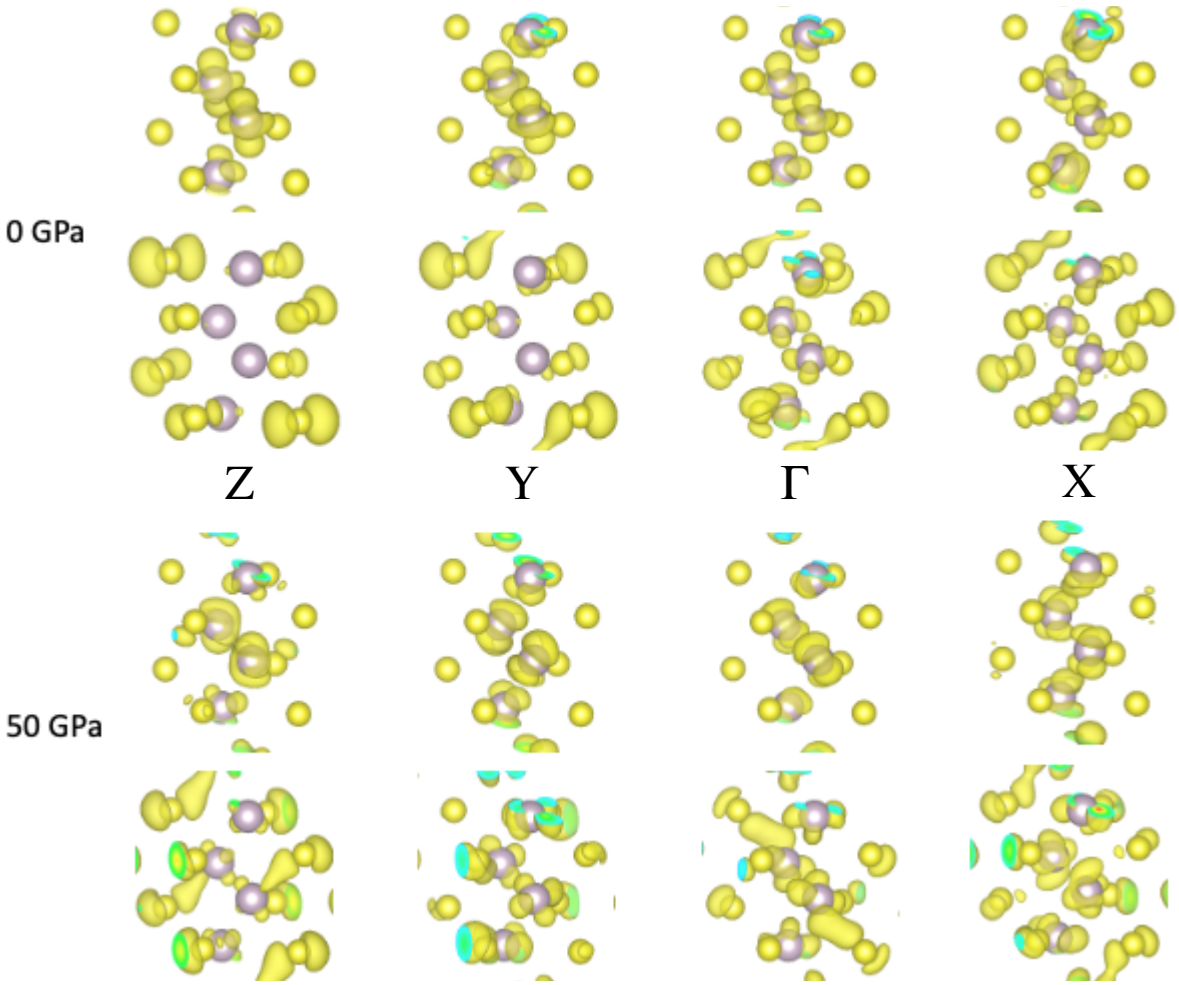

Figure S11: $\vec{k}$-point decomposed isosurfaces at 0 and 50 GPa for select points along the high-symmetry pathway. The CBM (top rows) and VBM (bottom rows) are shown at both pressures.

Table S3: Measured and computed Raman frequencies of $P2_1/c$ TcS_2 at 30 GPa which are assigned irreducible representations, or gerade modes. A total of 18 gerade modes are assigned below ($9A_g$+$9B_g$). Calculations were performed using the SCAN+rVV10 functional.

Experiment		Calculated	
Center (cm^{-1})	Intensity (a.u.)	Center (cm^{-1})	IRREP
194.344	5115.91	194.825	B_g
205.384	401.112	198.781	A_g
219.818	3261.98	225.075	A_g
234.092	3261.98	226.417	B_g
303.738	9160.25	309.314	A_g
353.2	7679.69	312.933	B_g
370.105	1527.35	348.841	A_g
375.55	1084.02	350.899	B_g
421.178	7932.04	371.723	A_g
437.376	1678.58	375.724	B_g
455.952	1409.78	403.719	A_g
483.129	2845.04	430.080	B_g
512.57	718.046	434.997	A_g
524.415	2059.47	439.682	B_g
586.465	911.779	442.728	A_g
		472.209	B_g
		522.087	A_g
		591.681	B_g

Table S4: Unit cell edges as a function of pressure comparing the structures studied for both compression pathways up to 50 GPa.

	$P\bar{1}$			$P2_1/c$		
Pressure (GPa)	a	b (Å)	c	a	b (Å)	c
0	6.36	6.46	6.63	5.82	5.79	5.87
10	6.28	6.37	6.12	5.82	5.79	5.87
20	6.22	6.31	5.89	5.62	5.63	5.68
30	6.15	6.24	5.74	5.55	5.57	5.61
40	6.09	6.18	5.64	5.49	5.53	5.55
50	6.03	6.12	5.55	5.43	5.48	5.50

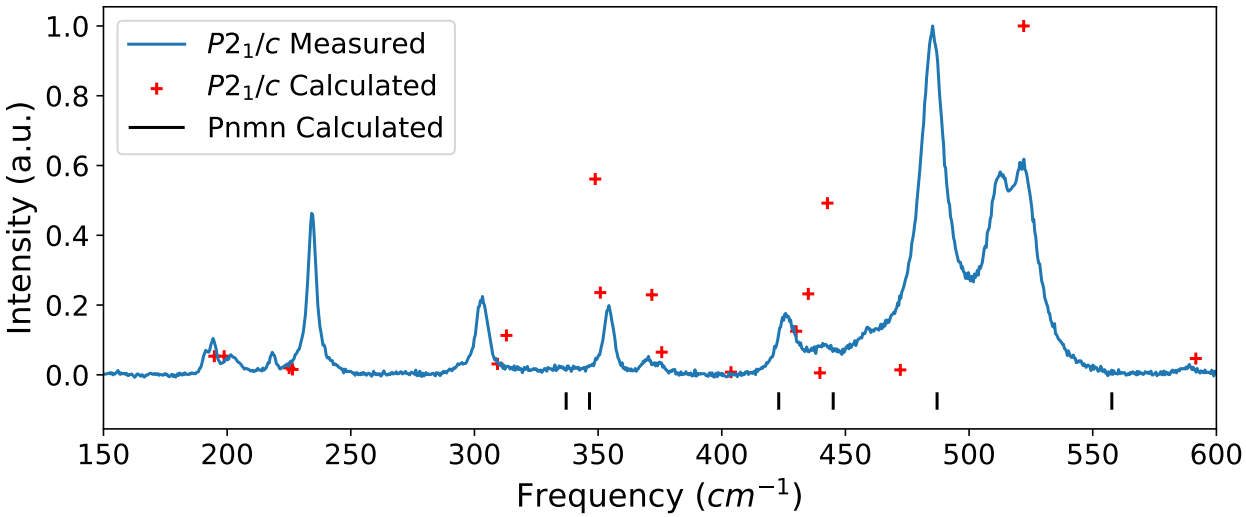

Figure S12: Comparison of the Raman spectra between the measured arsenopyrite phase (blue) and two calculated phases at 30 GPa. Calculated arsenopyrite is shown in red and marcasite in black. Unfortunately the calculation of Raman intensities in the latter phase is not possible.

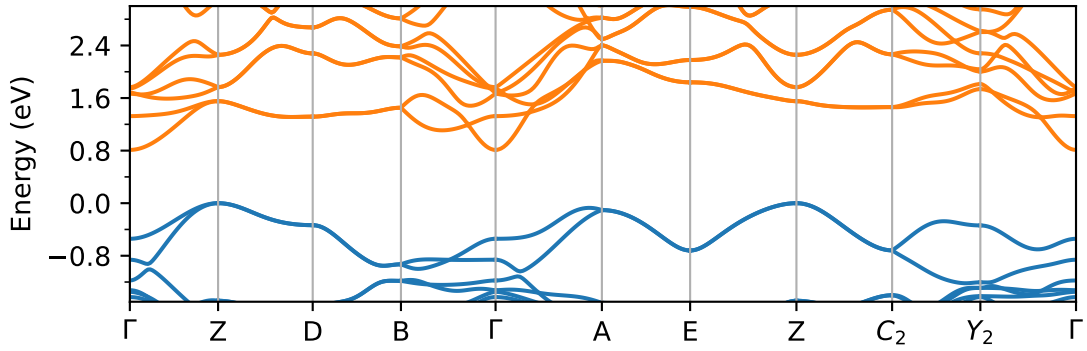

Figure S13: Electronic bandstructure of the $P2_1/c$ phase at 30 GPa. As can be seen, the difference between the electronic structure of this phase at 30 and 20 GPa is a minimal increase in the electronic bandgap, which is expected from the small structural change between these ionic structures. Notice also the preservation of the general shape for each band between the two phases.

References

(1) Siska, E.; Smith, D.; Childs, C.; Koury, D.; Forster, P. M.; Lawler, K. V.; Salamat, A. β-Technetium: An allotrope with a nonstandard volume-pressure relationship. *Physical Review Materials* **2021**, *5*, 063603.

(2) Ferrier, M.; Kerlin, W. M.; Poineau, F.; Sattelberger, A. P.; Czerwinski, K. R. Recent developments in the synthetic chemistry of technetium disulfide. *Dalton Trans.* **2013**, *42*, 15540–15543.

(3) Prescher, C.; Prakapenka, V. B. DIOPTAS: a program for reduction of two-dimensional X-ray diffraction data and data exploration. *High Pressure Res.* **2015**, *35*, 223–230.

(4) Toby, B. H.; Von Dreele, R. B. GSAS-II: the genesis of a modern open-source all purpose crystallography software package. *J. Appl. Crystallogr.* **2013**, *46*, 544–549.

(5) Joly, Y. X-ray absorption near-edge structure calculations beyond the muffin-tin approximation. *Phys. Rev. B* **2001**, *63*, 125120, DOI: 10.1103/PhysRevB.63.125120.

(6) Joly, Y.; Cavallari, C.; Guda, S. A.; Sahle, C. J. Full-Potential Simulation of X-ray Raman Scattering Spectroscopy. *J. Chem. Theory Comput.* **2017**, *13*, 2172, DOI: 10.1021/acs.jctc.7b00203.

(7) Oganov, A. R.; Lyakhov, A. O.; Valle, M. How Evolutionary Crystal Structure Prediction Works? @ Tand Why. *Accounts Chem. Res.* **2011**, *44*, 227, DOI: 10.1021/ar1001318.

(8) Oganov, A. R.; Glass, C. W. Crystal structure prediction using ab initio evolutionary techniques: Principles and applications. *The Journal of chemical physics* **2006**, *124*, 244704.

(9) Lyakhov, A. O.; Oganov, A. R.; Stokes, H. T.; Zhu, Q. New developments in evolutionary structure prediction algorithm USPEX. *Computer Physics Communications* **2013**, *184*, 1172–1182.

(10) Kresse, G.; Furthmüller, J. Efficient iterative schemes for ab initio total-energy calculations using a plane-wave basis set. *Phys. Rev. B* **1996**, *54*, 11169, DOI: 10.1103/PhysRevB.54.11169.

(11) Momma, K.; Izumi, F. *VESTA3* for three-dimensional visualization of crystal, volumetric and morphology data. *J. Appl. Crystallogr.* **2011**, *44*, 1272–1276, DOI: 10.1107/S0021889811038970.

(12) Peng, H.; Yang, Z.-H.; Perdew, J. P.; Sun, J. Versatile van der Waals Density Functional Based on a Meta-Generalized Gradient Approximation. *Phys. Rev. X* **2016**, *6*, 041005, DOI: 10.1103/PhysRevX.6.041005.

(13) Sun, J.; Ruzsinszky, A.; Perdew, J. P. Strongly Constrained and Appropriately Normed Semilocal Density Functional. *Phys. Rev. Lett.* **2015**, *115*, 036402, DOI: 10.1103/PhysRevLett.115.036402.

(14) Sabatini, R.; Gorni, T.; de Gironcoli, S. Nonlocal van der Waals density functional made simple and efficient. *Phys. Rev. B* **2013**, *87*, 041108, DOI: 10.1103/PhysRevB.87.041108.

(15) Perdew, J. P.; Burke, K.; Ernzerhof, M. Generalized gradient approximation made simple. *Physical review letters* **1996**, *77*, 3865.

(16) Blöchl, P. E. Projector augmented-wave method. *Phys. Rev. B* **1994**, *50*, 17953, DOI: 10.1103/PhysRevB.50.17953.

(17) Kresse, G.; Joubert, D. From ultrasoft pseudopotentials to the projector augmented-wave method. *Phys. Rev. B* **1999**, *59*, 1758–1775, DOI: 10.1103/PhysRevB.59.1758.

(18) Togo, A.; Tanaka, I. First principles phonon calculations in materials science. *Scr. Mater.* **2015**, *108*, 1–5.

(19) Glass, C. W.; Oganov, A. R.; Hansen, N. USPEX—Evolutionary crystal structure prediction. *Comput. Phys. Commun.* **2006**, *175*, 713, DOI: https://doi.org/10.1016/j.cpc.2006.07.020.

(20) Lamfers, H.-J.; Meetsma, A.; Wiegers, G.; de Boer, J. The crystal structure of some rhenium and technetium dichalcogenides. *J. Alloy Compd.* **1996**, *241*, 34, DOI: https://doi.org/10.1016/0925-8388(96)02313-4.

(21) Cococcioni, M.; De Gironcoli, S. Linear response approach to the calculation of the effective interaction parameters in the LDA+ U method. *Phys. Rev. B* **2005**, *71*, 035105.

(22) Dudarev, S.; Botton, G.; Savrasov, S.; Humphreys, C.; Sutton, A. Electron-energy-loss spectra and the structural stability of nickel oxide: An LSDA+ U study. *Phys. Rev. B* **1998**, *57*, 1505.

(23) Lawler, K. V.; Childs, B. C.; Mast, D. S.; Czerwinski, K. R.; Sattelberger, A. P.; Poineau, F.; Forster, P. M. Molecular and Electronic Structures of M_2O_7 (M = Mn, Tc, Re). *Inorg. Chem.* **2017**, *56*, 2448, DOI: 10.1021/acs.inorgchem.6b02503.

(24) Taylor, C. D. Oxidation of technetium metal as simulated by first principles. *The Journal of Physical Chemistry C* **2014**, *118*, 10017–10023.